metals

MDPI

Article

New Scanning Strategy Approach for Laser Powder Bed Fusion of Nd-Fe-B Hard Magnetic Material

Ivan A. Pelevin [1,*], Egor A. Terekhin [1], Dmitry Yu. Ozherelkov [1], Irina S. Tereshina [1,2], Dmitry Yu. Karpenkov [3], Fedor Yu. Bochkanov [4], Stanislav V. Chernyshikhin [1,5], Anton Yu. Nalivaiko [6] and Alexander A. Gromov [1]

1 Catalysis Lab, National University of Science and Technology MISIS, 119991 Moscow, Russia; terehinegor2016@gmail.com (E.A.T.); d.ozherelkov@gmail.com (D.Y.O.); irina_tereshina@mail.ru (I.S.T.); stanislav.chernyshikhin@skoltech.ru (S.V.C.); a.gromov@misis.ru (A.A.G.)
2 Faculty of Physics, Lomonosov Moscow State University, 119991 Moscow, Russia
3 Department of Magnetism, Lomonosov Moscow State University, 119991 Moscow, Russia; karpenkov_d_y@mail.ru
4 Department of Functional Nanosystems and High-Temperature Materials, National University of Science and Technology MISIS, 119991 Moscow, Russia; bochkanov_fy@mail.ru
5 Center for Materials Technologies, Skolkovo Institute of Science and Technology, 121205 Moscow, Russia
6 Directorate of Science, Moscow Polytechnic University, 107023 Moscow, Russia; a.y.nalivajko@mospolytech.ru
* Correspondence: i.pelevin@misis.ru

Abstract: Volumetric cubic and cylindrical samples from MQP-S Nd-Fe-B-type material were 3D-printed using the LPBF technique. Two different scanning strategies were used: the convenient single laser exposure scanning strategy and the newly proposed double scanning strategy aimed at improving the melting process and increasing the density of the synthesized material. Samples with a relative density value higher than 95% were obtained using the new scanning strategy by reducing void volume and cracks. This was achieved by decreasing internal stresses and reducing the tendency to form and propagate cracks. The double scanning strategy of half laser power followed by full power exposure provides higher magnetic properties (both coercive force and remanence). The coercive force increases with energy input decrease, while remanence has inverse dependence.

Keywords: laser powder bed fusion; selective laser melting; hard magnetic material; permanent magnet; rare earth intermetallic; 3D printing; $Nd_2Fe_{14}B$; scanning strategy

check for updates

Citation: Pelevin, I.A.; Terekhin, E.A.; Ozherelkov, D.Y.; Tereshina, I.S.; Karpenkov, D.Y.; Bochkanov, F.Y.; Chernyshikhin, S.V.; Nalivaiko, A.Y.; Gromov, A.A. New Scanning Strategy Approach for Laser Powder Bed Fusion of Nd-Fe-B Hard Magnetic Material. *Metals* **2023**, *13*, 1084. https://doi.org/10.3390/met13061084

Academic Editor: Zhongwu Liu

Received: 6 May 2023
Revised: 27 May 2023
Accepted: 6 June 2023
Published: 7 June 2023

Copyright: © 2023 by the authors. Licensee MDPI, Basel, Switzerland. This article is an open access article distributed under the terms and conditions of the Creative Commons Attribution (CC BY) license (https://creativecommons.org/licenses/by/4.0/).

1. Introduction

The development of new technological methods such as additive manufacturing (AM) in general and laser powder bed fusion (LPBF) in particular expands the scope of metal products design, allowing the synthesis of new complex-shaped structures with specific microstructure due to high cooling rates [1]. Structural materials such as aluminum [2,3], titanium [4,5], nickel alloys [6,7], and steels [8,9] were the first to be adopted into different additive technologies. LPBF of materials with different specific physical properties (electric, magnetic, thermal, etc.) is a relatively new scientific direction but it is attracting more and more attention. A transition material with both structural and functional properties could be nitinol, which possesses both high mechanical and functional (shape-memory) properties [10].

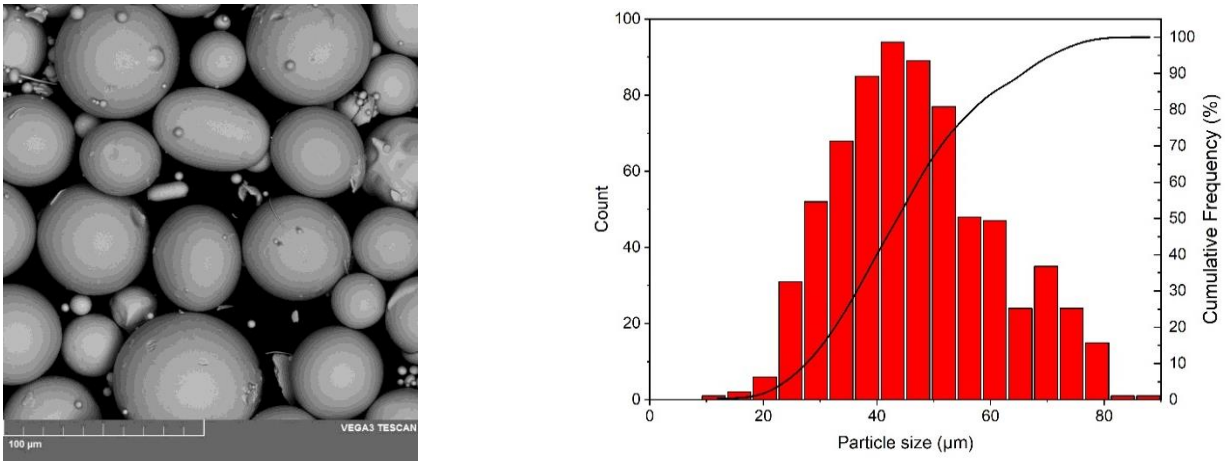
During each LPBF process, scanning strategies have to be set, i.e., trajectory of the laser spot on the powder layer. There are numerous different scanning strategies that have been developed for different materials to improve density, control texture and anisotropy, make uniform microstructure, change properties, etc. [11–15]. The effect of the scanning strategy on the structure and properties is explained by the different melting and heating histories of the powder layer [16,17]. Thus, varying the scanning strategy is a well-known and strong means to obtain the desired material properties.

A recent idea about 3D-printing permanent magnet (PM) with almost any shape is becoming a reality and will be a current topic for the coming years because of increasing demand for strong PMs. In terms of rare earth-based magnets (REM), their synthesis from magnetic powder with a binder is well known and has been studied in detail [18,19], whereas the novel synthesis of bulk REMs using the LPBF technique needs scientific effort to overcome the unresolved issues of low magnetic properties and structural defects. Some progress has been achieved so far. For example, 3D-printing Nd-Fe-B material without any binder through the LPBF technique was first claimed by Jacimovic et al. [20] about 5 years ago. Cubic samples and ring-like samples with complex shapes and a relative density (RD) of 92% were synthesized. Microstructure investigations showed the presence of cracks, pores, and voids, resulting in relatively low RD. However, the fundamental possibility of LPBF applied to $Nd_2Fe_{14}B$-type material was demonstrated and proved. Moreover, the magnetic properties of the obtained samples demonstrated the great potential of such an approach. It should be noted that the field was developed largely due to the appearance of a suitable raw powder—MQP-S-11-9-20001 grade by Magnequench [21] with spherical-shaped particles and low narrow particle size distribution providing good flowability and tap density [22], which are essential for the LPBF process. Few further scientific groups became involved in the research topic [23–32]. Optimization of the LPBF synthesis parameters allowed researchers to significantly increase the magnetic properties [23,28]. However, they were still far from being achieved through conventional methods. The main reasons for this are (i) the relatively low density due to different defects such as pores, voids, and cracks and (ii) the absence of any magnetic texture, resulting primarily in low remanence. A step forward was made through the introduction of different low-melt eutectics, firstly through the additional grain boundary infiltration process after LPBF performed by Huber et al. [26]. Then, mixing of the initial Nd-Fe-B powder with eutectic powder was carried out with a further LPBF process by Volegov et al. [29], reducing the number of technological steps. The second significant approach of high magnetic property achievement is connected with another composition of the alloy compared with MQP-S material. Goll et al. [30] compared RE-lean, stoichiometric, and over-stoichiometric Nd-Pr-Zr-Ti-Co-Fe-B compositions and reached a high (BH)max. However, the authors concluded that optimization of the LPBF parameters is still needed for the aim of decreasing porosity and fracture behavior and improving microstructure. The latest study by Tosoni et al. [32] describes the development of Cu-rich Nd-Fe-B alloy and powder. The authors showed that even non-spherical initial powder of the developed alloy allowed them to reach impressive results in terms of coercivity enhancement, but still with insufficient remanence. There is only one study that concerns scanning strategy variation during LPBF of Nd-Fe-B-based materials; namely, Goll et al. [33] showed that a specific non-rotating scanning strategy could help with texture formation. In other studies, the most common (67-degree rotation between adjacent layers) strategy is usually used.

Thus, despite the trend of new alloy composition findings, there is still no full solution for LPBF process optimization in terms of increasing the relative density of the printed materials to avoid pores, cracks, and other defects along with the formation of the desirable microstructure. An investigation of the double-exposure scanning strategy during the LPBF process was performed in the current study to get closer to fully dense and nearly defect-free Nd-Fe-B-based 3D-printed material. For this purpose, MQP-S spherical powder was chosen as the most convenient, predictable, and reproducible material with high processability for LPBF. The current study is the development of the research described in [22], which was focused on single-track synthesis. The double-exposure scanning strategy was used for the first time and applied to Nd-Fe-B-based materials, allowing a significant increase in the material density. Furthermore, an evaluation of the magnetic properties was performed to determine further areas of study with the aim of obtaining high-energy permanent magnets through the LPBF method.

2. Materials and Methods

Gas-atomized Nd-Fe-B powder (MQP-S-11-9-20001 grade purchased from Magnequench, Tianjin, China) [21] was used as an initial material. The initial powder had the following chemical composition, wt%: Fe 68.6%, B 2.7%, Ti 2.1%, Co 2.9%, Zr 4.7%, Pr 1.9%, Nd 17.0%, and less than 0.1% of other impurities. The powder had a spherical shape and the following size distribution: D10 = 26 μm, D50 = 45 μm, and D90 = 67 μm (see Figure 1).



(**a**) (**b**)

Figure 1. Initial Nd-Fe-B powder analysis: (**a**) SEM image; (**b**) particle size distribution.

Particle size distribution was determined using the laser diffraction method on an Analysette 22 NanoTecPlus device (FRITSCH GmbH, Idar-Oberstein, Germany) with a full-scale range of 0.01–2000 μm. Chemical composition, powder morphology, and microstructure characterization were performed using a scanning electron microscope (SEM) TESCAN Vega 3 (TESCAN, Brno, Czech Republic) with an X-ray energy dispersive microanalysis system (EDX) "Oxford Instruments Advanced Aztec Energy" (Oxford Instruments NanoAnalysis, High Wycombe, UK). The following SEM parameters were set during characterization: BSE mode with 20 kV voltage, 15 mm focusing distance. The emission current for the saturated filament was in the range of (60–90) μA. X-ray diffraction analysis (XRD) was carried out on a Rigaku Ultima IV X-ray diffractometer (Rigaku, Tokyo, Japan) using CrKα radiation (λ = 2.2936 Å). Microstructure analysis was evaluated on polished samples using a Carl Zeiss Axio Observer A1m (Oberkochen, Baden-Württemberg, Germany) optical microscope. The sample preparation consisted of mechanical grinding with a set of SiC papers (from 600 to 2500 grit) and final polishing using colloidal silica (3 μm and 0.25 μm).

The optimization of process parameters was performed through volumetric energy density (ED_V, J/mm^3) of the printing process:

$$ED_V = \frac{P}{V \cdot h \cdot t} \quad (1)$$

where P is the laser power (W), V is the laser scan speed (mm·s^{-1}), h is the hatch distance between neighboring laser scan tracks (mm), and t is the nominal layer or slicing thickness (μm), respectively. The optimization aims to maximize the relative material density, considering the specific volumetric energy input E_V into the material.

The relative material density (RD, %) was measured through the Archimedes method using an Adventurer Pro analytical balance with a measurement error of 0.001 g. The density was calculated using the following equation:

$$\rho_{sample} = \frac{m_{air}}{m_{air} - m_{liquid}} \left(\rho_{liquid} - \rho_{air} \right) + \rho_{air} \quad (2)$$

where m_{air} is the mass of the sample in the air, m_{liquid} is the mass of the sample fully submerged in isopropyl alcohol, and ρ_{liquid} and ρ_{air} are liquid and air densities in measurement conditions, respectively. Three measurements were made to determine the masses of the samples in air and liquid. The relative density was calculated against a theoretical density of 7.43 g·cm^{-3} for the Nd-Fe-B alloy [21].

Hysteresis loops were measured on cylindrical samples using a MagEq 201 induction magnetometer (AMT&C, Moscow, Russia) at room temperature and were corrected to the demagnetizing factor. The source of the magnetic field used in the magnetometer consisted of two concentrically arranged magnetic cylinders. The field in the internal cavity of the source is the vector sum of the fields created by each of the cylinders. The magnetic cylinders are connected to the stepper motor in such a way that when the motor rotates, the cylinders rotate synchronously in opposite directions. As a result, the field in the working area can vary from −18 to +18 kOe. The measuring system consists of two coils (measuring and compensation). The axes of the coils are parallel to the lines of the magnetic field. The samples were placed in the measuring coil and magnetized along its axis. Preliminarily, the samples were magnetized in an impulse magnetic field of 12 T along the building direction and cylinder axis.

An AddSol D50 machine (AddSol, Moscow, Russia) equipped with a continuous-wave (CW) ytterbium fiber laser (IPG Photonics, Oxford, MA, USA) of 400 W power with a 1064 nm wavelength and 80 μm laser spot size was used for the LPBF process. All samples were manufactured in an argon atmosphere on the steel substrate without preheating.

Two benchmarks of samples were obtained within a single LPBF procedure. The first type of sample was used for measurements of density and defect analysis and had the shape of a cube with a 5 mm edge length (see Figure 2). The raster scanning strategy demonstrated in Figure 2 was employed with the Meader-off mode (termination of laser influence during the laser turning). Perimeter scan and chess division were excluded from the strategy to eliminate the possible influence of overlays and offsets on the analysis. The scan pattern rotated 67° from layer to layer. One sample per set of parameters was printed. The second type of sample was represented by cylinders with a diameter of 1.2 mm and a height of 4.3 mm. The shape and dimensions of samples were dictated by the requirements of the magnetometer utilized for magnetic properties evaluation. The contour-based scanning strategy was used for cylindrical samples, as demonstrated in Figure 2. The distance between contours was equal to the hatch distance in the case of cubes (100 μm). It is known [34] that the contour-based scanning strategy is preferable over the rastering for objects with a small feature size. In this work, to obtain highly dense 3D-printed material, a strategy of double-scanning each layer was used to enhance the fusion of the brittle magnetic alloy. The double-scanning strategy means double exposure to the laser irradiation of the same scanning tracks. One exposure was performed on full laser power, whereas the other one was on half power. Both of the exposures were used to find the optimal printing parameters, and the experiment was performed twice. All given values are average values calculated after analysis of both samples. It should be noted that the second scan follows the same pattern as the first; thus, the hatching direction in the case of cubic samples did not change. The same layer thickness t = 30 μm and hatch spacing h = 100 μm were used as in the first experiment.

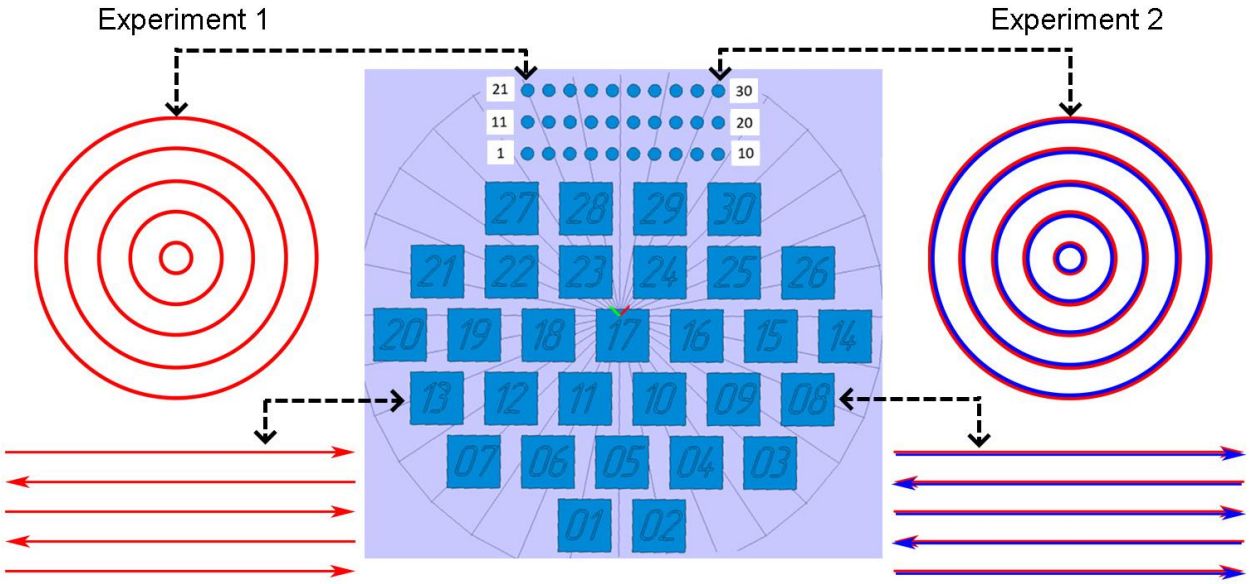


Figure 2. Nd-Fe-B samples form: Layout of samples on the substrate (in the middle); single-exposure scanning strategy (left—Experiment 1); double-exposure scanning strategy (right—Experiment 2).

3. Results

The first printing experiment was performed using a single-scanning strategy (see Figure 3). The *RD* of cubic samples was analyzed using the hydrostatic weighing method since it demonstrates high accuracy and allows us to obtain *RD* values of the whole object but not only from the current cross-section, which implies a metallographic method. Moreover, the preparation of the polished surface is a complicated task due to the high brittleness of the material and its tendency to crumble. Specifically, it concerns samples synthesized with non-optimal LPBF parameters. These crumbled brittle pieces not only leave voids but also lead to scratch formation that obstructs structure analysis. Moreover, due to the high brittleness of the material, only part of the samples was successfully separated from the baseplate for analysis without destruction. The measured *RD* values of samples printed at this stage are presented in Table 1.

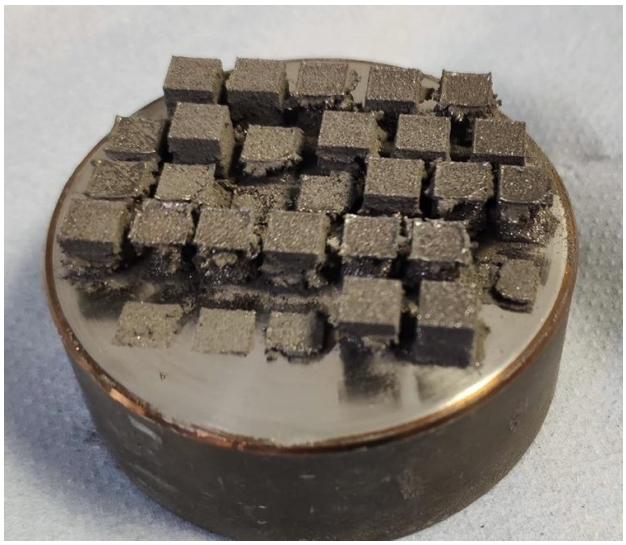


Figure 3. Nd-Fe-B cubic samples printed with the single-scan strategy.

Table 1. LPBF process parameters of the first experiment (single exposure) and RD values of the printed samples.

Sample	*P*, W	*V*, mm/s	ED_V, J/mm^3	*RD*, %
1.1	100	200	166.67	Destroyed
1.2	150	300	166.67	Destroyed
1.3	200	400	166.67	Destroyed
1.4	250	500	166.67	Destroyed
1.5	250	700	119.05	Destroyed
1.6	200	600	111.11	Destroyed
1.7	150	500	100	Destroyed
1.8	250	900	92.59	Destroyed
1.9	100	400	83.33	Destroyed
1.10	200	800	83.33	Destroyed
1.11	250	1100	75.76	Destroyed
1.12	150	700	71.43	Destroyed
1.13	200	1000	66.67	Destroyed
1.14	250	1300	54.10	Destroyed
1.15	100	600	55.56	Destroyed
1.16	150	900	55.56	Destroyed
1.17	200	1200	55.56	Destroyed
1.18	250	1500	55.56	61.3 ± 3.1
1.19	250	1700	49.02	Destroyed
1.20	200	1400	47.62	Destroyed
1.21	150	1100	45.45	55.4 ± 2.0
1.22	250	1900	43.87	54.8 ± 2.1
1.23	100	800	41.67	Destroyed
1.24	200	1600	41.67	48.2 ± 1.9
1.25	150	1300	38.46	45.3 ± 1.1
1.26	200	1800	37.04	63.4 ± 3.3
1.27	100	1000	33.33	48.0 ± 0.9
1.28	150	1500	33.33	55.4 ± 2.4
1.29	150	1700	29.41	55.6 ± 2.7
1.30	100	1200	27.78	52.0 ± 2.1
1.31	100	1400	23.81	54.8 ± 2.6
1.32	100	1600	20.83	48.1 ± 1.4

As seen from Table 1, half of the samples synthesized with the single-exposure scanning strategy could not be examined because of destruction during their separation from the substrate. The rest of the samples, which retained their shape, have insufficient density. However, some trends and dependencies can be noticed. The highest *RD* values were found for samples 1.18 and 1.26 (61.3 and 63.4%, respectively). These samples were printed with the highest laser power employed (200–250 W) and high scanning speeds of 1500–1800 mm/s, which resulted in volumetric energy densities of 37.0 and 55.6 J/mm^3, respectively. Such energy input values are in good agreement with the results shown by Bittner et al. [24] regarding process parameters and with the results shown by Huber et al. [26] regarding average RD values. Analysis of the measured RD values shows a trend of them increasing with ED_V in the 20–56 J/mm^3 range, whereas a further increase in energy input led to severe embrittlement, which destroyed the samples. Increasing the energy density means melt pool depth increasing, i.e., a greater volume of material is melted at each point in time with subsequent rapid solidification. A thin solidification layer experiences less residual stress and, thus, cracks and defects, whereas increasing the melting pool volume leads to a reverse effect.

A smaller depth of the melting pool provides more rapid solidification, forming a finer grain structure of the material, which is beneficial for high magnetic properties [30]. An analysis of Figure 4 shows that *RD* dependences on both laser power and scanning speed have a large spread. General tendencies of *RD* increasing with *P* and *V* can be noticed; however, the results of the experiment are not stable and the observed tendencies could be

accidental. The observed trend of *RD* via ED_V is more clear and is formed by two competing components: *RD* increasing with ED_V due to better melting and residual stress and defects also increasing with *EDv*, whereas the first component dominates in the mentioned range of ED_V = 20–56 J/mm^3. Thus, ED_V ~56 J/mm^3 is a boundary value limiting the process parameters' window from above. According to these results, the process window during the second experiment was limited by this ED_V value (see Table 1).

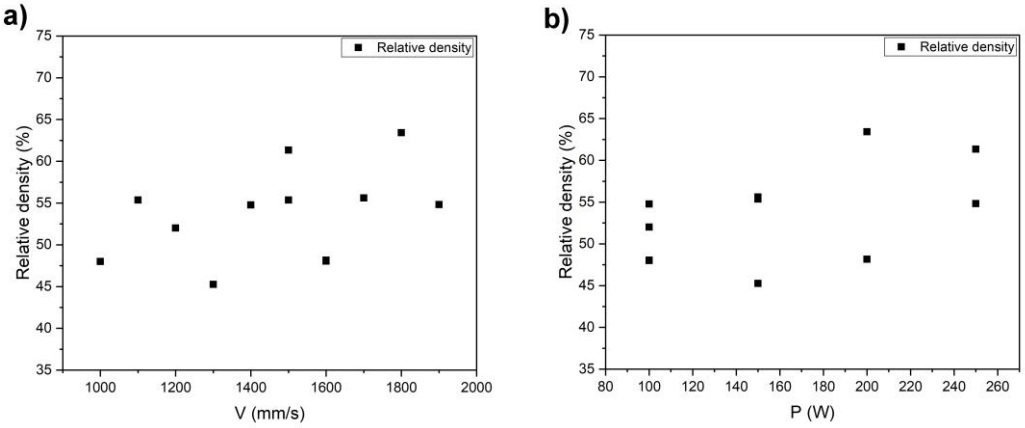
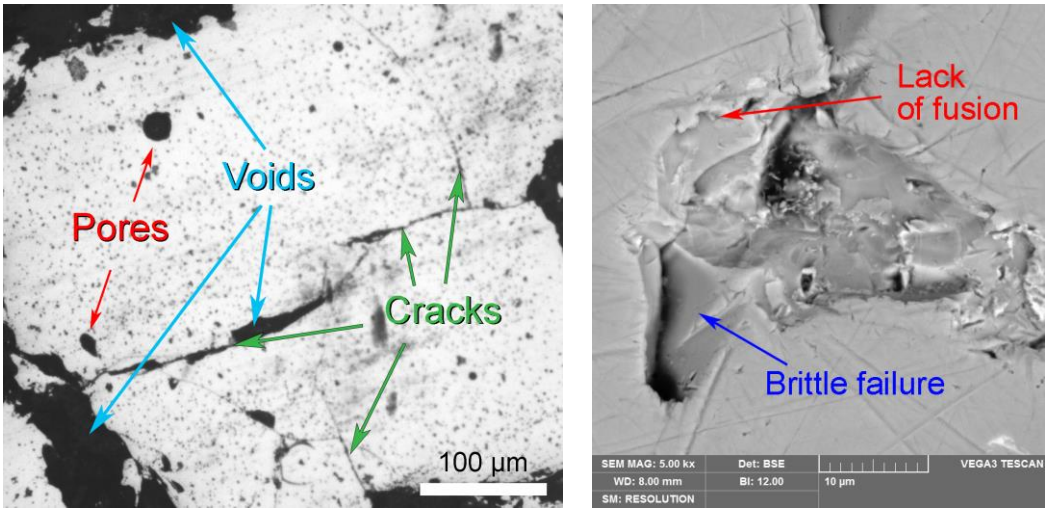


Figure 4. *RD* dependences on the laser power (**a**) and scanning speed (**b**) for the samples printed during the first experiment.

The observed defects are formed due to different reasons. The polished surface of the printed sample in Figure 5a shows a typical pattern of defects present. Usually, the most common defects in LPBFed materials are pores and cracks, which is also the case for the studied Nd-Fe-B material. Examples of typical pores are highlighted by red arrows in Figure 5a. This type of defect always arises in 3D-printed metallic materials due to the peculiarities of the technological process, but in the current case, it makes a small contribution to the whole level of defects. The main contribution is made by the areas that could be named lack-of-fusion zones (highlighted by blue arrows in Figure 5a). The presence of such zones is typical for the studied material and connected with two main factors: (i) the low processability of the material for the LPBF process and (ii) its high brittleness, leading to fracture of the material volume during sample preparation. This can be seen more clearly in the SEM image in Figure 5b. The edges of the void have different natures. Flat surfaces of cleavages indicate brittle failure (highlighted by blue arrows) and zones with rounded influxes indicate a lack of fusion (highlighted by red arrows). It can be assumed that failure and breaking off of the material with subsequent void formation starts from the lack-of-fusion area, with subsequent chipping during polishing. Cracks that arise due to the high material brittleness along with the high level of residual stress also contribute to the total defect volume. Such cracks are inherent in the LPBF method due to the rapid solidification of the material.



(**a**) (**b**)

Figure 5. The surface of the polished Nd-Fe-B samples obtained in the first experiment: (**a**) optical microscopy of the sample 1.18; (**b**) SEM of the fractured region.

In summary, obtaining fully dense volumetric objects for the Nd-Fe-B alloy, which is one of the basic conditions of high magnetic property realization, is difficult using a simple LPBF approach that usually works for high-processability materials such as aluminum alloys and others. As mentioned in the introduction, there are several possibilities for overcoming this difficulty: (i) adapting the chemical composition of the printed alloy to increase its LPBF processability [32]; (ii) addition of treatments and/or phases [26,29]; (iii) thorough LPBF process optimization including scanning strategy. It is expected that the combination of these approaches along with the finding of the method to create textured material during LPBF will lead to desirable results. However, efforts for every single approach are desired. A double-scan strategy could be an effective approach, helping to solve the problem of low density/high volume of defects in the LPBFed Nd-Fe-B volumetric objects. Figure 6 demonstrates cubic and cylindrical samples printed on a stainless steel baseplate as part of the current study according to the printing parameters and RD values represented in Table 2.



Figure 6. Cubic and cylindrical Nd-Fe-B samples printed with the double-scan strategy.

Table 2. LPBF process parameters of the second experiment (double exposure) and *RD* values of printed samples.

Sample №	First Exposure			Second Exposure			Summary	*RD*, %
	P, W	*V*, mm/s	ED_V, J/mm^3	*P*, W	*V*, mm/s	ED_V, J/mm^3	ED_V, J/mm^3	
2.1	250	1500	55.56	125	1500	27.78	83.34	93.0 ± 1.9
2.2	250	1700	49.02	125	1700	24.51	73.53	96.0 ± 1.8
2.3	200	1400	47.62	100	1400	23.81	71.43	85.8 ± 0.9
2.4	150	1100	45.45	75	1100	22.725	68.18	86.8 ± 1.0
2.5	250	1900	43.87	125	1900	21.935	65.81	88.7 ± 1.4
2.6	100	800	41.67	50	800	20.835	62.51	86.0 ± 1.1
2.7	200	1600	41.67	100	1600	20.835	62.51	86.6 ± 1.7
2.8	150	1300	38.46	75	1300	19.23	57.69	86.4 ± 1.9
2.9	200	1800	37.04	100	1800	18.52	55.56	85.1 ± 1.5
2.10	100	1000	33.33	50	1000	16.665	50.00	91.4 ± 2.0
2.11	150	1500	33.33	75	1500	16.665	50.00	83.4 ± 0.7
2.12	150	1700	29.41	75	1700	14.705	44.12	80.3 ± 1.0
2.13	100	1200	27.78	50	1200	13.89	41.67	75.4 ± 2.9
2.14	100	1400	23.81	50	1400	11.905	35.72	75.9 ± 3.0
2.15	100	1600	20.83	50	1600	10.415	31.25	75.0 ± 2.7
2.16	125	1500	27.78	250	1500	55.56	83.34	87.7 ± 1.3
2.17	125	1700	24.51	250	1700	49.02	73.53	88.2 ± 1.3
2.18	100	1400	23.81	200	1400	47.62	71.43	86.7 ± 1.0
2.19	75	1100	22.725	150	1100	45.45	68.18	92.4 ± 1.8
2.20	125	1900	21.935	250	1900	43.87	65.81	89.0 ± 1.6
2.21	50	800	20.835	100	800	41.67	62.51	88.4 ± 1.5
2.22	100	1600	20.835	200	1600	41.67	62.51	84.4 ± 1.0
2.23	75	1300	19.23	150	1300	38.46	57.69	86.2 ± 1.2
2.24	100	1800	18.52	200	1800	37.04	55.56	83.1 ± 0.8
2.25	50	1000	16.665	100	1000	33.33	50.00	81.4 ± 0.9
2.26	75	1500	16.665	150	1500	33.33	50.00	78.7 ± 1.6
2.27	75	1700	14.705	150	1700	29.41	44.12	82.7 ± 1.5
2.28	50	1200	13.89	100	1200	27.78	41.67	89.5 ± 1.1
2.29	50	1400	11.905	100	1400	23.81	35.72	77.2 ± 2.1
2.30	50	1600	10.415	100	1600	20.83	31.25	72.8 ± 2.0

The main qualitative result of the double-scan strategy is seen in Table 2—all printed samples retain the shape, i.e., no sample was destroyed even after separation from the baseplate. Moreover, the *RD* values measured for all cubic samples are far higher than the best results obtained using the single-scanning strategy. A deeper analysis of the *RD* value dependences on printing parameters showed a correlation with the first experiment, namely that *RD* tends to increase with ED_V regardless of the subsequent exposures (full- and half-power), as seen in Figure 7.

The obtained effect of *RD* increase through the double-scanning strategy can be explained by temperature history features that the material undergoes during the printing process. Firstly, let us discuss subsequent full- and half-power exposure (samples 2.1–2.15). In this case, the first full-power exposure repeats the single-exposure experiment, which gave insufficient results, with the additional half-power treatment during the second scanning. The latter implies remelting of the already melted layer, wherein the depth of the remelted layer is less than the depth of the melted one. As was mentioned above, this means that less melt volume exists at every moment of the process; thus, the solidification rate increases (resulting in finer grain structure) and less residual stress occurs (reducing defects volume), providing dense layer formation. When the printing of the next layer starts, partial remelting of the previous layer occurs, leading to strong bonding between layers.

In the case of subsequent half- and full-power exposures (samples 2.16–2.30), the printing process starts from semi-sintering using a preliminary scan. This resulted in low-density material with numerous voids and unmelted volumes, along with poor bonding between the current and previous layers. Subsequent remelting under full-power laser irradiation during the second scanning affects not only the current layer but also part of the previous layer, leading to strong bonding formation. The melting of the preliminary semi-sintered layer occurs more easily due to the higher thermal conductivity of such

material compared with the powder. Moreover, such a scanning strategy forms a more optimal microstructure, providing higher magnetic properties that will be discussed below.

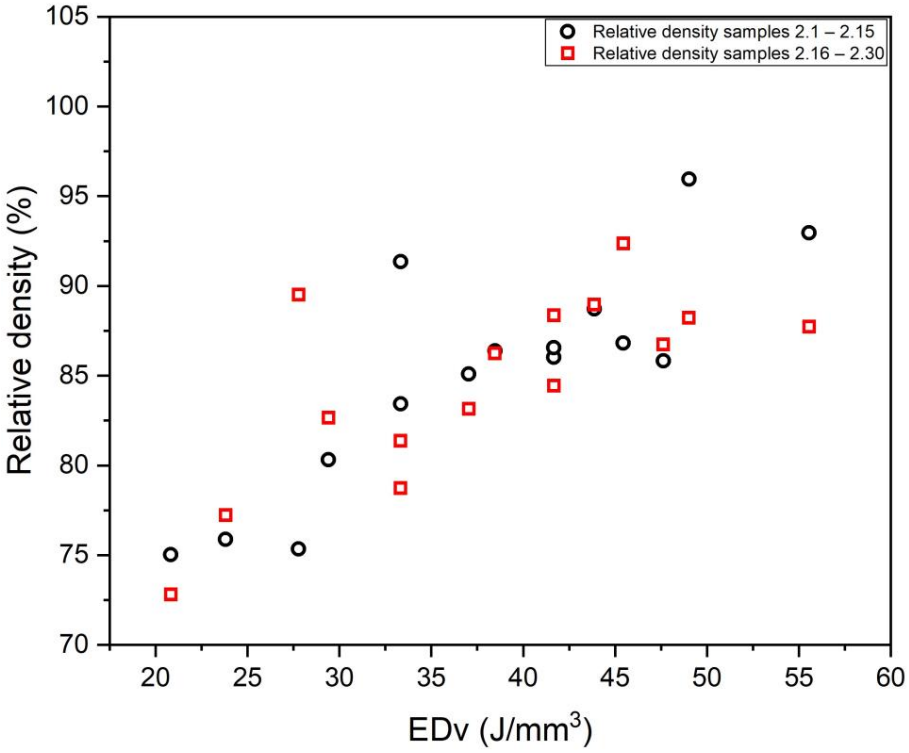
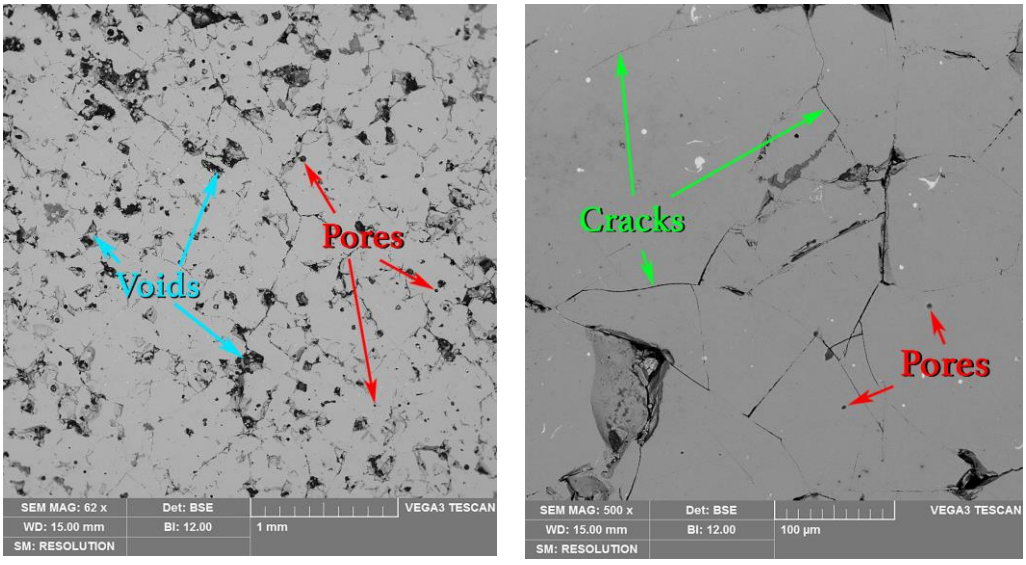


Figure 7. Nd-Fe-B samples' *RD* dependence on volumetric energy density after LPBF with double-scan strategy.

All these processes in general lead to a much better melting process during the second experiment, resulting in higher *RD* and lower levels of defects compared with the single-scanning strategy, as seen in Figure 8. The average values of *RD* of both sets of samples are almost the same (85.0 and 84.5%).



(**a**) (**b**)

Figure 8. The polished surface of sample 2.2 obtained using SEM: (**a**) general view with 62× magnification; (**b**) detailed view with 500× magnification.

A comparison of the samples from the two experiments with the single- and double-scanning strategies shows a significant difference between them besides just the proportion of voids areas and dense material. The number and size of cracks (green arrow) are far lower after double-scan strategy synthesis, along with an absence of unmelted particles present in the material synthesized with the single-scanning strategy. The geometry of pores (red arrow) and voids (blue arrow) is similar in both experiments, mostly because of the material properties and its behavior under laser irradiation. More detailed SEM analysis with a higher magnification of samples from the double-scanning strategy was performed and is shown in Figure 8b. the LPBF method implies layer-by-layer crystallization with high temperature gradients within small volumes; thus, cold cracks usually arise in the case of brittle, low-plasticity materials. Cracks observed in the current study correspond to cold breakage, i.e., crack formation occurs in already solidified material because of melt crystallization on its surface and internal stress. As can be seen, cracks propagate mostly straightforwardly, presumably through grains but not along grain boundaries. Thus, it can be concluded that the melting process provides strong enough intergrain bonding, leading to a more energetically favorable way of crack propagation through a brittle bulk material.

Another feature of the observed structure is the presence of white inclusions (see Figures 8b and 9a). EDX analysis of such inclusions indicates high concentrations of Nd and oxygen and low iron content within these areas (see Figure 9b–d). Thus, these inclusions are a neodymium oxide, and the shape of their solidification is interesting. Rounded, liquid-like shapes denote that the oxide inclusions solidify firstly within the melt. XRD shows the presence of a small volume of the Nd_2O_3 phase (see XRD pattern in Figure 9e). Since the melting temperature of the Nd_2O_3 is 2233 °C [35], it can be concluded that the temperature within the melt pool is higher, which is in good agreement with corresponding experiments [1,36]. Despite the higher energy input in the case of Al-based materials during LPBF, the temperature of the melt pool in the case of $Nd_2Fe_{14}B$ 3D printing could be even higher due to the low absorption (high reflectivity) of laser irradiation by aluminum. The rounded shape of oxide inclusions may occur in the case of their formation and crystallization within the liquid, whereas disrupted shapes with thin shapes could occur in the case of non-crystallized oxide pulling towards the melt pool boundary. It should be noted that the formation of the oxides is observed because of oxygen's presence in the initial powder material, presumably originating during being in the air.

A possible solution to prevent oxide formation could be vacuum heat treatment of the initial powder, but since the employed 3D-printer design features do not allow us to proceed without contact of the powder with air, such treatment seems useless. However, an additional separate study concerning this point is needed.

The hysteresis loops of the printed cylindrical samples were measured to evaluate their main magnetic properties and their dependences on the printed parameters. It should be noted that just an evaluation of magnetic properties is provided to outline further research with their detailed analysis. Figure 10 shows the demagnetization curves of some samples. It is seen that the coercive force and remanence of samples printed with different parameters differ significantly. For example, the H_C of sample 2.29 is twice as high as that of 2.16 despite the similar scanning strategy, but inversely correlates with ED_V, which, for sample 2.29, is more than two times lower than for 2.16.

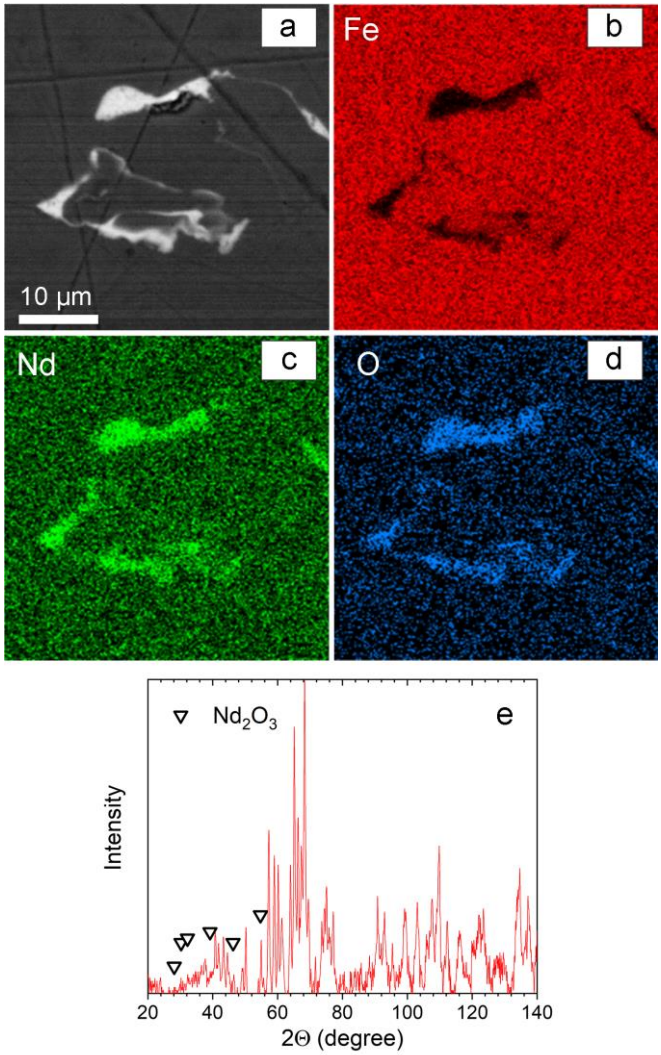


Figure 9. EDX analysis (**a**–**d**) and XRD pattern (**e**) of the Nd-Fe-B sample 2.2.

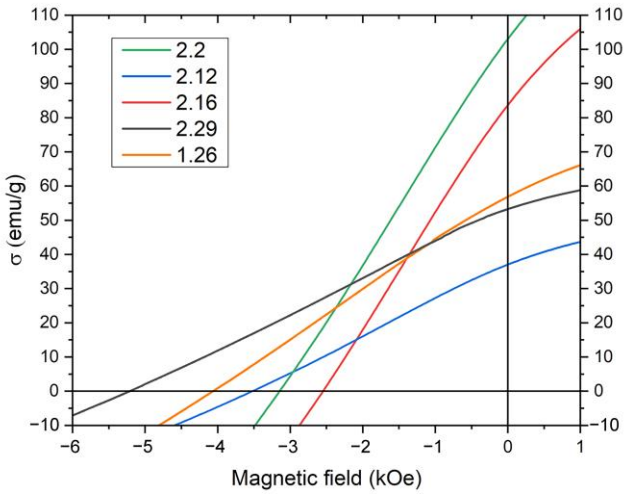


Figure 10. Demagnetization curves of different printed Nd-Fe-B cylindrical samples.

Absolute values of remanence vary in a wide range from 35.6 to 105.1 emu/g, wherein the σ_{max}/σ_r ratio of all samples is similar and lies in the vicinity of 0.6, which more or less corresponds to isotropic magnetic material without strong texture. The hysteresis loop of

sample 1.26 (with H_C = 4.2 kOe and σ_r = 57 emu/g) does not fundamentally differ from the loops of double-scanning samples (2.12 and 2.29 in Figure 10), whereas taking into account the difference in density, the strength of the magnetic field generated by a unit volume of material will differ significantly. Sample 2.2 shows the highest remanence of more than 105 emu/g, which is almost two times higher than for sample 1.26. All curves could be divided into two types: (1) curves 2.2 and 2.16 with higher remanence and lower H_C and (2) the remaining curves with lower σ_r and higher H_C (an example of these curves is presented in Figure 11). It should be noted that the demagnetization curves of all samples are smooth without inflections, which means that samples consist of a single magnetic phase, i.e., no phase decomposition occurred during the LPBF process. This conclusion is also confirmed by XRD analysis (see Figure 9e).

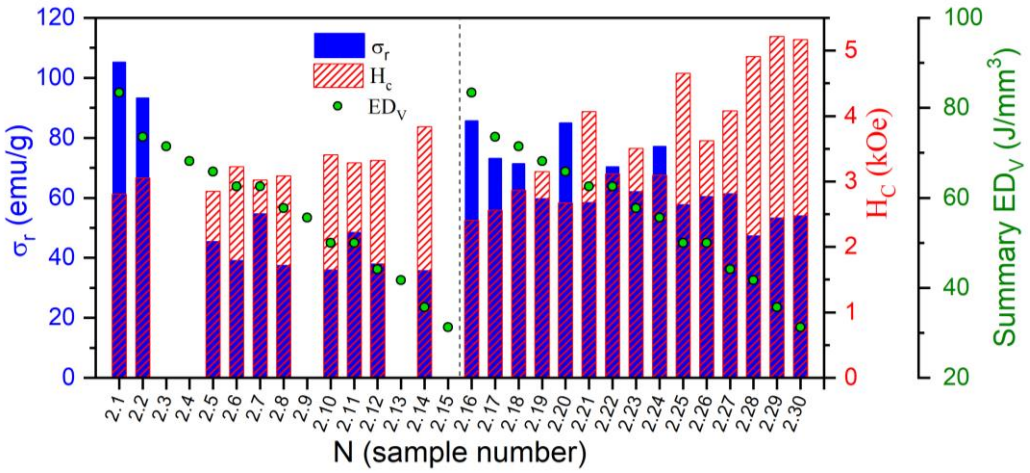


Figure 11. Diagram of remanence and coercive force values of Nd-Fe-B samples printed using double-scanning strategy.

A comparative diagram showing the σ_r and H_C of all the measured samples printed using the double-scanning strategy is presented in Figure 11 to find the trends and dependences of these magnetic characteristics on printing parameters. Summary ED_V values are also depicted in the same figure. Data gaps in the diagram mean that corresponding samples were destroyed during measurements. The trend of coercive force increasing with summary ED_V decreasing is visible, i.e., it increases from sample 2.1 to 2.15 and from 2.16 to 2.30. There are some fluctuations, but the tendency is clear, especially for the second set of samples. The highest H_C values around 5 kOe were measured for samples 2.28–2.30. The highest H_C in the first set of samples was 3.84 kOe (sample 2.14 synthesized with low ED_V). An inverse tendency is observed for remanence, which correlates with RD dependence. The highest σ_r values were obtained for the first samples from both sets (2.1–2.2 and 2.16–2.20). This tendency is especially clear for the first set, whereas the remanence in the second set varies in a smaller range.

The average levels of both coercive force and remanence of the second sample set (half- and full-power exposure) are noticeably higher than those of the first one, which indicates better microstructure formation during LPBF with such a scanning strategy. It should be noted that the level of the obtained magnetic properties is still an order lower than industrially produced magnets, and there is still a long way to go to approach them using the LPBF technique [37]. However, the obtained properties are comparable with those achieved by other scientific groups using the LPBF method and MQP-S powder without eutectic phases. The coercive force values in the current study are slightly lower than those obtained by Bittner et al. [24], but approximately equal to or even higher than those achieved by Skalon et al. [27] and Goll et al. [30]. Herein, the achieved values of *RD* and magnetization have higher remanence than in the literature [32]. A more detailed

study of magnetic properties' dependences on printing parameters and possible ways to increase them is planned to be presented in future works.

4. Conclusions

The convenient single-laser exposure scanning strategy of MQP-S $Nd_2Fe_{14}B$-type material 3D-printing using the LPBF technique was compared with the newly proposed double-scanning strategy. Two sets of samples were printed during the double-scanning procedure: (1) full-power laser exposure with subsequent half-power and (2) half-power preliminary exposure with subsequent full-power scanning. The new scanning strategy provided a better melting process, leading to higher *RD* of the synthesized material. High-density samples with *RD* values up to 96% were obtained due to reducing the volume of voids and cracks. The double-scanning strategy with different energy inputs allowed us to decrease internal stresses and to reduce the tendency of formation and propagation of cracks in a brittle material. The proposed scanning strategy does not lead to undesirable phase formation, i.e., no iron phase formation was observed during LPBF. The presence of some amount of oxygen in the initial powder material led to the formation of neodymium oxide inclusions. Despite the comparable results of the *RD* of both sets of samples, the strategy with half- and full-power exposures provides higher magnetic properties (both coercive force and remanence). The tendency of coercive force increasing with summary ED_V decrease was observed for both sets, whereas inverse dependences were found for remanence. Samples printed with higher ED_V have higher remanence with lower H_C, and vice versa; samples printed with low ED_V show lower remanence with higher H_C values. Thus, a new scanning strategy of the LPBF process was proposed as a way to increase the density of 3D-printed Nd-Fe-B hard magnetic material.

Author Contributions: Conceptualization, I.A.P. and A.A.G.; methodology, I.S.T., S.V.C. and D.Y.O.; investigation, E.A.T., D.Y.K., A.Y.N. and F.Y.B.; data curation, I.A.P. and I.S.T.; writing—original draft preparation, I.A.P. and E.A.T.; writing—review and editing, D.Y.O. and A.A.G.; visualization, I.A.P., E.A.T., D.Y.O., A.Y.N. and I.S.T.; supervision, A.A.G. All authors have read and agreed to the published version of the manuscript.

Funding: This research was funded by the Russian Science Foundation (RSF), grant number 21-79-10239.

Data Availability Statement: The data presented in this study are available on request from the corresponding author. The data are not publicly available due to privacy.

Acknowledgments: The work was supported in part by M.V. Lomonosov Moscow State University Program of Development (MSU, Russia). Also, authors would like to thank N.Y. Pankratov and M.V. Lyange for assistance.

Conflicts of Interest: The authors declare no conflict of interest.

References

1. Pelevin, I.A.; Nalivaiko, A.Y.; Ozherelkov, D.Y.; Shinkaryov, A.S.; Chernyshikhin, S.V.; Arnautov, A.N.; Zmanovsky, S.V.; Gromov, A.A. Selective Laser Melting of Al-Based Matrix Composites with Al_2O_3 Reinforcement: Features and Advantages. *Materials* **2021**, *14*, 2648. [CrossRef] [PubMed]
2. Aboulkhair, N.T.; Simonelli, M.; Parry, L.; Ashcroft, I.; Tuck, C.; Hague, R. 3D printing of Aluminium alloys: Additive Manufacturing of Aluminium alloys using selective laser melting. *Prog. Mater. Sci.* **2019**, *106*, 100578. [CrossRef]
3. Aboulkhair, N.T.; Everitt, N.M.; Maskery, I.; Ashcroft, I.; Tuck, C. Selective laser melting of aluminum alloys. *MRS Bull.* **2017**, *42*, 311–319. [CrossRef]
4. Maskery, I.; Aremu, A.O.; Simonelli, M.; Tuck, C.; Wildman, R.D.; Ashcroft, I.A.; Hague, R.J.M. Mechanical Properties of Ti-6Al-4V Selectively Laser Melted Parts with Body-Centred-Cubic Lattices of Varying cell size. *Exp. Mech.* **2015**, *55*, 1261–1272. [CrossRef]
5. Simonelli, M.; Tse, Y.Y.; Tuck, C. On the Texture Formation of Selective Laser Melted Ti-6Al-4V. *Metall. Mater. Trans. A* **2014**, *45*, 2863–2872. [CrossRef]
6. Choi, J.-P.; Shin, G.-H.; Yang, S.; Yang, D.-Y.; Lee, J.-S.; Brochu, M.; Yu, J.-H. Densification and microstructural investigation of Inconel 718 parts fabricated by selective laser melting. *Powder Technol.* **2017**, *310*, 60–66. [CrossRef]
7. Zhang, D.; Feng, Z.; Wang, C.; Wang, W.; Liu, Z.; Niu, W. Comparison of microstructures and mechanical properties of Inconel 718 alloy processed by selective laser melting and casting. *Mater. Sci. Eng. A* **2018**, *724*, 357–367. [CrossRef]

8. Garibaldi, M.; Ashcroft, I.; Lemke, J.N.; Simonelli, M.; Hague, R. Effect of annealing on the microstructure and magnetic properties of soft magnetic Fe-Si produced via laser additive manufacturing. *Scr. Mater.* **2018**, *142*, 121–125. [CrossRef]
9. Garibaldi, M.; Ashcroft, I.; Simonelli, M.; Hague, R. Metallurgy of high-silicon steel parts produced using Selective Laser Melting. *Acta Mater.* **2016**, *110*, 207–216. [CrossRef]
10. Taheri Andani, M.; Saedi, S.; Turabi, A.S.; Karamooz, M.R.; Haberland, C.; Karaca, H.E.; Elahinia, M. Mechanical and shape memory properties of porous $Ni_{50.1}Ti_{49.9}$ alloys manufactured by selective laser melting. *J. Mech. Behav. Biomed. Mater.* **2017**, *68*, 224–231. [CrossRef]
11. Vikram, R.J.; Gokulnath, S.A.; Prashanth, K.G.; Suwas, S. Effect of scanning strategy on microstructure and texture evolution in a selective laser melted Al-33Cu eutectic alloy. *J. Alloys Compd.* **2023**, *936*, 168098. [CrossRef]
12. Pant, P.; Salvemini, F.; Proper, S.; Luzin, V.; Simonsson, K.; Sjöström, S.; Hosseini, S.; Peng, R.L.; Moverare, J. A study of the influence of novel scan strategies on residual stress and microstructure of L-shaped LPBF IN718 samples. *Mater. Des.* **2022**, *214*, 110386. [CrossRef]
13. Zhou, L.; Sun, J.; Bi, X.; Chen, J.; Chen, W.; Ren, Y.; Niu, Y.; Li, C.; Qiu, W.; Yuan, T. Effect of scanning strategies on the microstructure and mechanical properties of Ti-15Mo alloy fabricated by selective laser melting. *Vacuum* **2022**, *205*, 111454. [CrossRef]
14. Zhang, C.; Ozcan, H.; Xue, L.; Atli, K.C.; Arróyave, R.; Karaman, I.; Elwany, A. On the effect of scan strategies on the transformation behavior and mechanical properties of additively manufactured NiTi shape memory alloys. *J. Manuf. Process.* **2022**, *84*, 260–271. [CrossRef]
15. Hu, Z.; Yang, Z.; Du, Z.; Wu, J.; Dong, J.; Wang, H.; Ma, Z. Effect of scanning strategy on the anisotropy in microstructure and properties of Cu-Cr-Zr alloy manufactured by laser powder bed fusion. *J. Alloys Compd.* **2022**, *920*, 165957. [CrossRef]
16. Wang, Y.; Ji, X.; Liang, S.Y. Analytical modeling of temperature distribution in laser powder bed fusion with different scan strategies. *Opt. Laser Technol.* **2023**, *157*, 108708. [CrossRef]
17. Zhang, W.; Tong, M.; Harrison, N.M. Scanning strategies effect on temperature, residual stress and deformation by multi-laser beam powder bed fusion manufacturing. *Addit. Manuf.* **2020**, *36*, 101507. [CrossRef]
18. Wang, H.; Lamichhane, T.N.; Paranthaman, M.P. Review of additive manufacturing of permanent magnets for electrical machines: A prospective on wind turbine. *Mater. Today Phys.* **2022**, *24*, 100675. [CrossRef]
19. Chaudhary, V.; Mantri, S.A.; Ramanujan, R.V.; Banerjee, R. Additive manufacturing of magnetic materials. *Prog. Mater. Sci.* **2020**, *114*, 100688. [CrossRef]
20. Jaćimović, J.; Binda, F.; Herrmann, L.G.; Greuter, F.; Genta, J.; Calvo, M.; Tomše, T.; Simon, R.A. Net Shape 3D Printed NdFeB Permanent Magnet. *Adv. Eng. Mater.* **2017**, *19*, 1700098. [CrossRef]
21. MQP-S-11-9-20001. Available online: https://mqitechnology.com/product/mqp-s-11-9-20001/ (accessed on 1 September 2021).
22. Pelevin, I.A.; Ozherelkov, D.Y.; Chernyshikhin, S.V.; Nalivaiko, A.Y.; Gromov, A.A.; Chzhan, V.B.; Terekhin, E.A.; Tereshina, I.S. Selective laser melting of Nd-Fe-B: Single track study. *Mater. Lett.* **2022**, *315*, 131947. [CrossRef]
23. Bittner, F.; Thielsch, J.; Drossel, W.-G. Microstructure and magnetic properties of Nd-Fe-B permanent magnets produced by laser powder bed fusion. *Scr. Mater.* **2021**, *201*, 113921. [CrossRef]
24. Bittner, F.; Thielsch, J.; Drossel, W.-G. Laser powder bed fusion of Nd–Fe–B permanent magnets. *Prog. Addit. Manuf.* **2020**, *5*, 3–9. [CrossRef]
25. Kolb, T.; Huber, F.; Akbulut, B.; Donocik, C.; Urban, N.; Maurer, D.; Franke, J. Laser Beam Melting of NdFeB for the production of rare-earth magnets. In Proceedings of the 2016 6th International Electric Drives Production Conference, EDPC 2016, Nuremberg, Germany, 30 November–1 December 2016.
26. Huber, C.; Sepehri-Amin, H.; Goertler, M.; Groenefeld, M.; Teliban, I.; Hono, K.; Suess, D. Coercivity enhancement of selective laser sintered NdFeB magnets by grain boundary infiltration. *Acta Mater.* **2019**, *172*, 66–71. [CrossRef]
27. Skalon, M.; Görtler, M.; Meier, B.; Arneitz, S.; Urban, N.; Mitsche, S.; Huber, C.; Franke, J.; Sommitsch, C. Influence of melt-pool stability in 3D printing of ndfeb magnets on density and magnetic properties. *Materials* **2020**, *13*, 139. [CrossRef] [PubMed]
28. Urban, N.; Huber, F.; Franke, J. Influences of process parameters on rare earth magnets produced by laser beam melting. In Proceedings of the 2017 7th International Electric Drives Production Conference (EDPC), Würzburg, Germany, 5–6 December 2017; pp. 1–5.
29. Volegov, A.S.; Andreev, S.V.; Selezneva, N.V.; Ryzhikhin, I.A.; Kudrevatykh, N.V.; Mädler, L.; Okulov, I.V. Additive manufacturing of heavy rare earth free high-coercivity permanent magnets. *Acta Mater.* **2020**, *188*, 733–739. [CrossRef]
30. Goll, D.; Trauter, F.; Bernthaler, T.; Schanz, J.; Riegel, H.; Schneider, G. Additive Manufacturing of Bulk Nanocrystalline FeNdB Based Permanent Magnets. *Micromachines* **2021**, *12*, 538. [CrossRef]
31. Maltseva, V.E.; Andreev, S.V.; Neznakhin, D.S.; Urzhumtsev, A.N.; Selezneva, N.V.; Volegov, A.S. The Magnetic Properties of a NdFeB Permanent Magnets Prepared by Selective Laser Sintering. *Phys. Met. Metallogr.* **2022**, *123*, 740–745. [CrossRef]
32. Tosoni, O.; Mendonça, E.B.; Reijonen, J.; Antikainen, A.; Schäfer, L.; Riegg, S.; Gutfleisch, O. High-coercivity copper-rich Nd-Fe-B magnets by powder bed fusion using laser beam method. *Addit. Manuf.* **2023**, *64*, 103426. [CrossRef]
33. Goll, D.; Trauter, F.; Loeffler, R.; Gross, T.; Schneider, G. Additive Manufacturing of Textured FePrCuB Permanent Magnets. *Micromachines* **2021**, *12*, 1056. [CrossRef]
34. Duong, E.; Masseling, L.; Knaak, C.; Dionne, P.; Megahed, M. Scan path resolved thermal modelling of LPBF. *Addit. Manuf. Lett.* **2022**, *3*, 100047. [CrossRef]

35. David, E.; Lide, R. *CRC Handbook of Chemistry and Physics, Internet Version 2007*, 87th ed.; Taylor & Francis: Boca Raton, FL, USA, 2007.
36. Liao, H.; Zhu, H.; Xue, G.; Zeng, X. Alumina loss mechanism of Al_2O_3-AlSi10 Mg composites during selective laser melting. *J. Alloys Compd.* **2019**, *785*, 286–295. [CrossRef]
37. Coey, J.M.D. Perspective and Prospects for Rare Earth Permanent Magnets. *Engineering* **2020**, *6*, 119–131. [CrossRef]

Disclaimer/Publisher's Note: The statements, opinions and data contained in all publications are solely those of the individual author(s) and contributor(s) and not of MDPI and/or the editor(s). MDPI and/or the editor(s) disclaim responsibility for any injury to people or property resulting from any ideas, methods, instructions or products referred to in the content.